We are IntechOpen, the world's leading publisher of Open Access books Built by scientists, for scientists

4,800
Open access books available

122,000
International authors and editors

135M
Downloads

Our authors are among the

154
Countries delivered to

TOP 1%
most cited scientists

12.2%
Contributors from top 500 universities

WEB OF SCIENCE™

Selection of our books indexed in the Book Citation Index in Web of Science™ Core Collection (BKCI)

Interested in publishing with us?
Contact book.department@intechopen.com

Numbers displayed above are based on latest data collected.
For more information visit www.intechopen.com

16

Control of Polymorphism and Mass-transfer in Al_2O_3 Scale Formed by Oxidation of Alumina-Forming Alloys

Satoshi Kitaoka, Tsuneaki Matsudaira and Masashi Wada
Japan Fine Ceramics Center
Japan

1. Introduction

Thermal barrier coatings (TBCs) are widely used for hot section components of gas turbine engines to protect the underlying metals from the high operating temperatures; they serve to both increase the engine efficiency and improve the durability of components. TBC systems typically consist of a Ni-based superalloy substrate, an alumina forming-alloy bond coat and an yttria-stabilized zirconia topcoat. When TBCs are exposed to high temperatures in oxidizing environments, a thermally grown oxide (TGO) develops on the bond coat surface underneath the top coat. Fracture of TBCs progresses in the vicinity of the TGO, which attains a critical thickness during thermal cycling operations (Evans et al., 2001). Thus, suppressing oxidation of the bond coat is anticipated to enhance the durability of TBCs.
Alumina-forming alloys tend to form metastable Al_2O_3 polymorphs such as gamma- and theta-phases in oxidizing environments at 1100-1450 K (Brumm et al., 1992, Tolpygo et al., 2000). The thermodynamically stable alpha-Al_2O_3 typically forms at longer oxidation times and/or higher temperatures. Metastable oxide scales consisting of the gamma- and theta-phases contain lattice defects so that they hardly act as a protective layer to further oxidation of the alloys compared with a alpha-Al_2O_3 scale (Brumm et al., 1992). It is also well known that the transformation of the alpha-phase from metastable polymorphs involves large changes in volume (~13%) and morphology.
Metastable oxides tend to form on the bond coat during coating with the topcoat in an oxygen-containing atmosphere at high temperatures, so that they are present at the interface between the bond coat and topcoat. The transformation of these oxides to the stable alpha-phase at higher operating temperatures promotes topcoat spalling. Thus, in order to enhance the durability of TBCs, the as-processed TBC microstructures should contain a thin layer of alpha-Al_2O_3 at the interface with no the metastable oxides. The standard grit-blasting procedure that is used in practical applications to prepare the bond coat for topcoat deposition promotes the formation of alpha-Al_2O_3. However, it also results in severe contamination of the coating surface and accelerates oxidation of the bond coat (Tolpygo et al., 2001). Some studies have revealed that a pre-oxidation step that forms a alpha-Al_2O_3 TGO on the bond coat without grit blasting reduces further oxidation of the bond coat and improves the durability of the TBC (Tolpygo et al., 2005, Nijdam et al., 2006, Matsumoto et al., 2006, 2008). Although it is generally preferable to perform pre-oxidation above 1450 K to produce a thin alpha-Al_2O_3 oxide and avoid producing metastable oxides, high temperature

treatment degrades the bond coat or causes excessive oxidation. Thus, pre-oxidation should be carried out at lower temperatures and with shorter oxidizing times to form a thin alpha-Al_2O_3 layer. Matsumoto et al. (2006, 2008) reported that pre-oxidation of CoNiCrAlY under a low oxygen partial pressure (P_{O2}) and at lower temperature of 1323 K for 4 h, for which thermodynamic calculations predict that only alpha-$(Al,Cr)_2O_3$ will be produced, resulted in the formation of a dense alpha-Al_2O_3 scale with large grains, which functioned as an excellent protective layer against further oxidation of the alloy. They also reported that the theta-phase remained when $(Co,Ni)(Al,Cr)_2O_4$ was produced by oxidation under a higher P_{O2}, despite using the same oxidizing time as that under the lower P_{O2}. These results suggest that reducing the P_{O2} in pre-oxidized environments accelerates the polymorph transformation to the alpha-phase, but the extent of this acceleration and its mechanism remain unclear.

It is well known that adding chromium or iron to alumina-forming alloys accelerates the transformation from metastable polymorphs to alpha-Al_2O_3 (Brumm et al., 1992, Pint et al., 1997, Peng et al., 2003). Because these isovalent ions, which are larger than Al^{3+}, can dissolve into both the metastable phases and the alpha-phase, they partially compensate for the dilatational stress field of the dislocation and transformation (Clarke, 1998). This may be why the transformation is accelerated by adding chromium or iron. By contrast, the transformation is retarded when gamma-Al_2O_3 powders are substituted with 0.1-0.5 mol% of divalent cations such as Co^{2+} or Ni^{2+} (Odaka et al., 2008). Doping gamma-Al_2O_3 with 5 mol% Ni^{2+} also increases the hydrothermal stability relative to non-doped gamma-Al_2O_3 (Nagano et al, 2008). They may be due to their poor solvencies in the alpha-phase, although the divalent cations are larger than Al^{3+} ions. Thus, it is anticipated that the polymorphism of the Al_2O_3 scale can be controlled by controlling the P_{O2} during the pre-oxidation step. In other words, the transformation is accelerated under lower P_{O2}, when both aluminum and chromium in the alloy are simultaneously oxidized to form alpha-$(Al,Cr)_2O_3$, but it may be retarded under higher P_{O2}, when cobalt and nickel in the alloy are oxidized in addition to aluminum and chromium, resulting in the formation of $(Co,Ni)(Al,Cr)_2O_4$. In this chapter, control of Al_2O_3 polymorph formation was verified by the oxidation of specific components in CoNiCrAlY under a thermodynamically determined P_{O2}, resulting in the rapid formation of a dense, smooth alpha-Al_2O_3 scale (Kitaoka et al., 2010).

Suppressing mass-transfer through the alpha-Al_2O_3 scale is also anticipated to further improve the durability of the TBCs. When oxidation of the alumina forming alloys takes place through alumina scale under higher oxygen partial pressures (P_{O2}), such as in air, an oxygen potential gradient is generally induced in the direction opposite to the aluminum potential gradient in accordance with the Gibbs-Duhem equation. Thus, the alumina scale is grown on the alloys by the inward grain boundary diffusion of oxygen and the outward grain boundary diffusion of aluminum, resulting in the development of the grain boundary ridges on the scale surfaces. By contrast, ridges do not form when oxidation is carried out through alumina scale in a low P_{O2} environment, such as in a purified argon flow (Nychka et al., 2005). The ridge formation mechanism (i.e., mass-transfer through the alumina scale) is thus thought to depend on the P_{O2}.

The inherent effectiveness of monolithic alumina as a barrier to oxygen permeation has been estimated directly by measuring oxygen permeation through a polycrystalline alumina wafer exposed to oxygen potential gradients at high temperatures, where the each surface of the wafer is deliberately subjected to different P_{O2} values (Matsudaira et al., 2008, Wada et al., 2008, Kitaoka et al., 2009, Volk et al., 1968, Courtright et al., 1992, Ogura et al., 2001). When the potential gradients are produced by a combination of high P_{O2} values, oxygen

permeates mainly via grain boundary diffusion of aluminum through aluminum vacancies from the lower to the higher P_{O2} surface, resulting in the formation of grain boundary ridges on the latter surface (Matsudaira et al., 2008, Wada et al., 2008, Kitaoka et al., 2009). In other words, O_2 molecules are adsorbed onto the surface at higher P_{O2} and subsequently dissociate into oxygen ions (forming alumina), whereas oxygen ions on the opposite surface at a lower P_{O2} are desorbed by association into O_2 molecules (decomposition of alumina). Conversely, under an oxygen potential gradient generated by a combination of low P_{O2} values, oxygen permeation occurs by grain boundary diffusion of oxygen through oxygen vacancies from the higher to the lower P_{O2} surface. In this case, very little ridge formation occurs at grain boundaries because of the very low aluminum flux (Kitaoka et al., 2009). Thus, the main diffusing species leading to oxygen permeation through the grain boundaries depends on the P_{O2} values producing the oxygen potential gradients. This readily explains the absence of grain boundary ridges on alumina scale formed under low P_{O2} conditions, such as in a purified argon flow (Nychka et al., 2005).

Many studies have focused on oxygen grain boundary diffusion in polycrystalline alumina using either secondary ion mass spectroscopy (SIMS) (Plot et al., 1996, Nakagawa et al., 2007, Messaoudi et al., 1998) or nuclear reaction analysis (NRA) (Heuer, 2008) to determine ^{18}O depth profiles after high temperature exchange with ^{18}O-enriched oxygen. Messaoudi et al. (1998) determined oxygen grain boundary diffusion coefficients during transport through a growing alumina scale. This was done by oxidizing alumina-forming alloys in a $^{16}O_2$ atmosphere, further oxidizing them in $^{18}O_2$ and then determining the ^{18}O distribution in the alumina scale using SIMS. The oxygen grain boundary diffusion coefficients measured by this procedure were larger than those determined from extrapolated diffusion data for polycrystalline alumina annealed in a homogeneous environment without any oxygen potential gradients (Plot et al., 1996, Nakagawa et al., 2007, Heuer, 2008). The corresponding activation energies (Messaoudi et al., 1998) derived using the double oxidation technique were smaller than those obtained by annealing (Plot et al., 1996, Nakagawa et al., 2007, Heuer, 2008). Kitaoka et al. (2009) have reported that the oxygen grain boundary diffusion coefficients, which were determined from the oxygen permeation coefficients of undoped polycrystalline alumina wafers exposed to oxygen potential gradients at high temperatures, decreased with increasing P_{O2}, and the corresponding activation energies were similar to those for the actual alumina scales formed on the alloys (Messaoudi et al., 1998). Thus, oxygen grain boundary diffusivity in polycrystalline alumina under oxygen potential gradients is apparently different from that in a homogeneous environment.

On the other hand, there has been only two reports of aluminum lattice diffusion coefficients determined using SIMS (Paladino et al., 1962, Le Gall et al., 1994). In this case, the appropriate tracer, ^{26}Al, has a very low specific activity and an extremely long half-life of 7.2×10^5 years, making it very difficult to perform radiotracer diffusion experiments. Recent studies have used Cr^{3+} instead of Al^{3+} as the diffusion species because of the extremely long half-life of the ^{26}Al isotope. Cr^{3+} is a suitable substitute for Al^{3+} because it has a similar ionic radius and is isovalent. For example, Bedu-Amissah et al. used a diffusion couple of alumina and chromia to measure grain boundary diffusion coefficients from Cr^{3+} concentration profiles obtained using an X-ray microprobe (Amissah et al., 2007). Kitaoka et al. (2009) have recently estimated aluminum grain boundary diffusion coefficients from the oxygen permeation coefficients of undoped polycrystalline alumina wafers exposed to oxygen potential gradients at high temperatures (Kitaoka et al., 2009). The aluminum grain boundary diffusion coefficients were found to increase with increasing P_{O2}, in an inverse relationship to the P_{O2} dependence of the oxygen grain boundary diffusion coefficients.

Alumina-forming alloys contain small quantities of oxygen-reactive elements (REs) (e.g., Y, La, Ti, Zr, and Hf) to improve the oxidation-resistance of the alloys. These REs segregate at grain boundaries in growing alumina scales during oxidation of the alloys. The obvious difficulty is that it is not known what the diffusing species along the grain boundaries in the scales might be. Nevertheless, the REs are speculated to inhibit the scale growth by effectively blocking the outward grain-boundary diffusion of aluminum due to an ionic size misfit, since the ionic sizes of the REs are larger than Al^{3+} (Nychka et al., 2005, Pint et al., 1998). However, during long-duration, high-temperature oxidation, REs that segregated at grain boundaries were found to diffuse toward the scale surfaces together with aluminum, resulting in the precipitation of RE-rich particles on the surfaces (Pint et al., 1998). This casts a doubt on the conjecture that the REs can effectively control the movement of aluminum. The coexistence of various kinds of REs further complicates the interpretation of the experimental results. On the other hand, rare earth doping can significantly increase the high-temperature creep resistance of polycrystalline alumina (Matsunaga et al., 2003, Ikuhara et al., 2001, Yoshida et al., 2002). Several studies have suggested that segregation of large dopant elements changes the grain boundary environment by 'site blocking' critical oxygen diffusion pathways (Amissah et al., 2007, Wang et al., 1999, Cho et al., 1999, Cheng et al., 2008, Priester, 1989, Korinek et al., 1994) and/or by strengthening grain boundaries by enhancing bond strengths in the vicinity of dopant ions (Yoshida et al., 2002, Buban et al., 2006).

As mentioned above, when undoped polycrystalline alumina wafers were exposed to oxygen potential gradients at high temperatures, the main diffusing species depended on P_{O2}. This phenomenon will be useful for elucidating how much the migration of oxygen and aluminum is affected by REs segregated at the grain boundaries.

In this chapter, the effect of lutetium doping on oxygen permeability in polycrystalline alumina wafers exposed to steep oxygen potential gradients was evaluated at high temperatures to investigate the mass-transfer phenomena through the scale (Matsudaira et al., 2010). It is well known that lutetium doping can significantly improve high-temperature creep resistance in polycrystalline alumina (Matsunaga et al., 2003, Ikuhara et al., 2001, Yoshida et al., 2002); therefore, it is also expected to retard mass-transfer in alumina under oxygen potential gradients.

2. Control of polymorphism in Al_2O_3 scale

2.1 Thermodynamic prediction of stable oxides

The P_{O2} dependence of equilibrium amounts and components of stable condensed oxide species are first estimated thermodynamically when CoNiCrAlY (Co-28%Ni-21%Cr-16%A-0.3%Y (in atomic %)) is exposed to an oxidizing environment at a high temperature. The equilibrium calculation was conducted using FactSage_free-energy minimization computer code together with a database for the Co-Ni-Cr-Al-Y-O system that mainly consists of the SGTE database and some solution models of condensed phases. The Redlich-Kister-Muggianu polynomial model was applied to solid solution phases such as the gamma-phase (alloy) and (Co,Ni)O, and multi-sublattice formalism to the beta-phase (alloy) and $(Co,Ni)(Al,Cr)_2O_4$. Subregular (Degterov et al., 1996) and sublattice (Ansara et al., 1997) models were used for $(Al,Cr)_2O_3$ and the gamma'-phase, respectively. Initial conditions for the calculation were 1 mol of CoNiCrAlY, a total pressure of 10^5 Pa (equal to the sum of partial pressures of O_2 and Ar), and a temperature of 1323 K.

Figure 1 shows the equilibrium amounts of the condensed species as a function of the equilibrium P_{O2} at 1323K. alpha-$(Al,Cr)_2O_3$ is thermodynamically stable under the

equilibrium P_{O2} below 10^{-9} Pa. On the contrary, $(Co,Ni)(Al,Cr)_2O_4$ and (Co,Ni)O are stable under the P_{O2} above 10^{-9} Pa and 10^{-5} Pa, respectively. All the yttrium in the alloy is also oxidized to produce about 10^{-3} mol of $Al_5Y_3O_{12}$ in the P_{O2} range shown in Fig. 1.

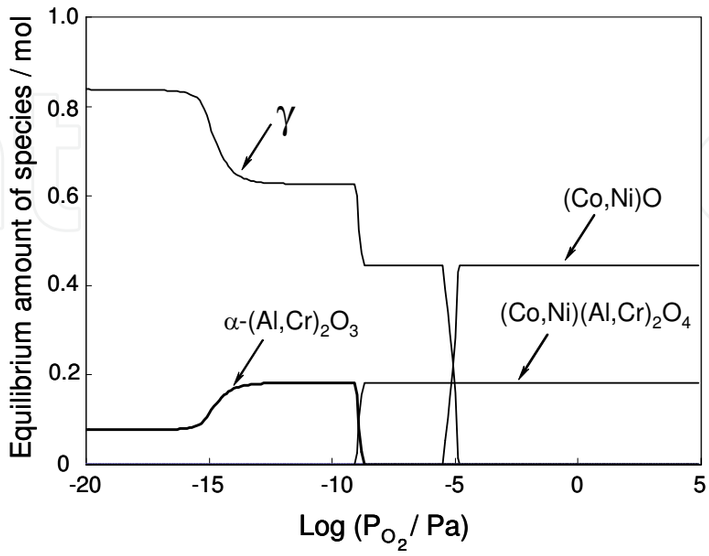

Fig. 1. Equilibrium amount of species as a function of partial pressure of O_2 (P_{O2}) at 1323 K for Co-0.28Ni-0.21Cr-0.16Al-0.003Y (at %). γ-phase represents a metallic phase.

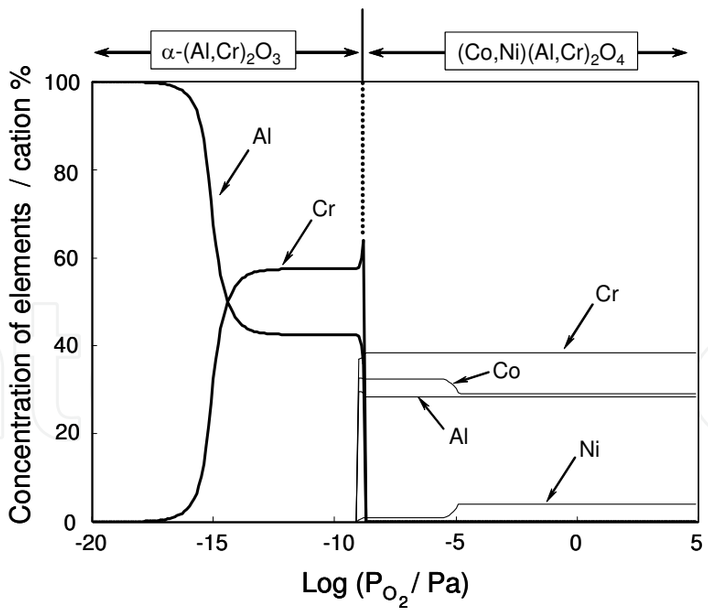

Fig. 2. Equilibrium concentration of each element in the solid solution phases of alpha-$(Al,Cr)_2O_3$ and $(Cr,Ni)(Al,Cr)_2O_4$ as a function of P_{O2} at 1323 K for Co-0.28Ni-0.21Cr-0.16Al-0.003Y (at %).

The equilibrium concentration of each element in the solid solution phases of alpha-$(Al,Cr)_2O_3$ and $(Cr,Ni)(Al,Cr)_2O_4$ as a function of P_{O2} at 1323 K for the CoNiCrAlY alloy is

shown in Fig. 2. For a P_{O2} below 10^{-9} Pa, where alpha-$(Al,Cr)_2O_3$ is thermodynamically stable, the concentration of chromium dissolved in the oxide increases sharply with an increase in P_{O2} above 10^{-17} Pa, up to about 60 cation % for a P_{O2} above 10^{-13} Pa. By contrast, for a P_{O2} above 10^{-9} Pa, at which $(Co,Ni)(Al,Cr)_2O_4$ is stable, both cobalt and nickel dissolve in the complex oxide in addition to aluminum and chromium.

In the actual system, it is speculated that initially amorphous and/or gamma-alumina, which can dissolve in oxides consisting of other elements such as chromium, and/or cobalt and nickel in the alloy, are produced at lower temperatures during heating in the oxidation treatment. This is followed by transformation into the theta-phase, and finally conversion into thermodynamically stable phases such as alpha-alumina and/or $(Co,Ni)(Al,Cr)_2O_4$ while holding at a higher temperature. Thus, the oxidation of the alloy under a P_{O2} at which both aluminum and chromium are oxidized and at which neither cobalt nor nickel is oxidized will accelerate transformation into the alpha-alumina phase. According to Figs. 1 and 2, a suitable P_{O2} for promoting the polymorph transformation lies below 10^{-9} Pa at 1323 K. By contrast, the transformation will be retarded in a P_{O2} above 10^{-9} Pa. In this chapter, control of Al_2O_3 polymorph formation was verified by the oxidation of CoNiCrAlY under a thermodynamically determined P_{O2} of 10^{-14} Pa at 1323 K, compared with oxidation under P_{O2} of 1 and 10^5 Pa (Kitaoka et al., 2010).

2.2 Experimental procedures

CoNiCrAlY alloy (Co-28%Ni-21%Cr-16%Al-0.3%Y (in atomic %)) was coated by vacuum plasma spraying to a thickness of 150 micrometer on a 20 × 40 × 2.5-mm grit-blasted substrate of Inconel 738LC and the alloy surface was then polished to Ra = 0.25 micrometer. Each sample was introduced into a V-notch with a radius of curvature below 20 micrometer on the substrate side to prepare the cross-section of the sample after the subsequent oxidation treatment by brittle fracture in liquid N_2. The V-notched samples were ultrasonically cleaned in acetone and dried at 393 K for 1 h. Each sample was set in a furnace, the internal atmosphere of which was replaced with either O_2, commercial Ar, or P_{O2} controlled Ar using a solid-state electrochemical oxygen pump system (Matsumoto et al., 2006, 2008). The gas flow rate was 3×10^{-4} m^3/min. The sample was heated to 1323 K at a rate of 5 K/min, and then held at the temperature for 10, 200, and 600 min, where the P_{O2} values were 10^5 Pa for O_2, 10 Pa for the commercial Ar, and 10^{-14} Pa for the controlled Ar. After that, the samples were cooled to room temperature at a rate of 5 K/min.

Crystalline phases in the scale formed by oxidation were identified by X-ray diffraction (XRD). Identification of Al_2O_3 polymorphs in the scale such as the theta- and alpha-phases was also performed by photostimulated Cr^{3+} luminescence spectroscopy (PSLS). The surface morphology and cross-sections of the scales were measured by scanning electron microscopy (SEM). Elemental depth profiles of the scale were measured by secondary ion mass spectrometry (SIMS).

2.3 Characteristics of oxide scales

The crystalline phases in the oxide scales, which were identified by XRD and PSLS, are summarized in Table 1. The higher the P_{O2} used for oxidation was, the longer the metastable theta-phase survived. The P_{O2} dependence for the formation of the oxide phases in the scale on oxidation time is in good agreement with the thermodynamic predictions shown in Fig. 1. This demonstrates that the oxidation of the alloy under a precisely regulated P_{O2} can be used to control the polymorphism of the Al_2O_3 scale.

Time/ min	Po_2 / Pa		
	10^{-14}	10	10^5
10	α-Al_2O_3	θ + α-Al_2O_3 $(Co,Ni)(Al,Cr)_2O_4$	θ + α-Al_2O_3 $(Co,Ni)(Al,Cr)_2O_4$
200	↓	α-Al_2O_3 $(Co,Ni)(Al,Cr)_2O_4$	↓
600	↓	↓	α-Al_2O_3 $(Co,Ni)(Al,Cr)_2O_4$

Table 1. Crystalline phases in the oxide scales.

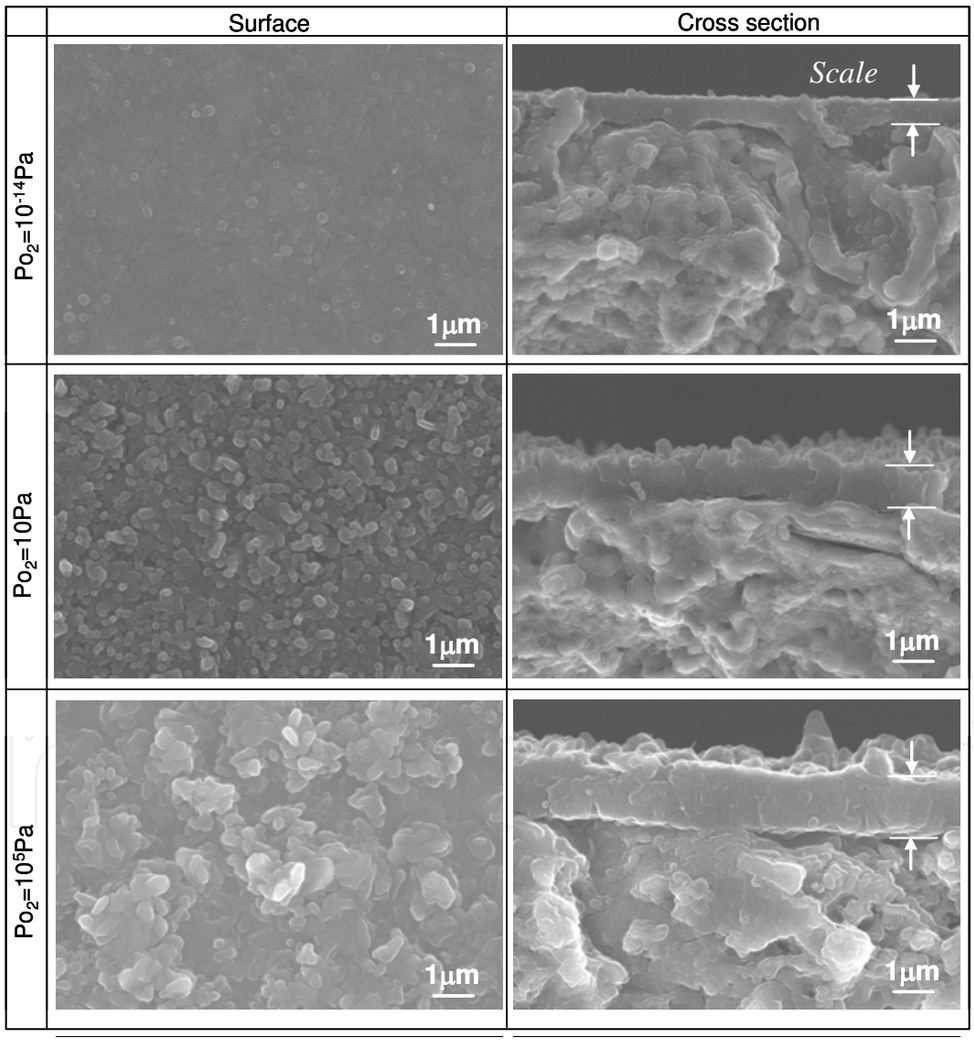

Fig. 3. SEM micrographs of the surfaces and cross-sections of the samples oxidized at 1323 K for 600 min under P_{O2} of 10^{-14}, 10, and 10^5 Pa.

The SEM micrographs of the surfaces and cross-sections of the samples oxidized at 1323 K for 600 min under P_{O2} of 10^{-14}, 10, and 10^5 Pa, respectively, are shown in Fig. 3. The surface

of the oxide scale formed under a P_{O2} of 10^{-14} Pa is relatively smooth and its thickness is about 1 micrometer. On the other hand, the higher the P_{O2} for the oxidation is, the larger the oxide crystals are which are exposed on the scales, increasing the density of surface irregularities. The scale thickness increases with an increase in P_{O2} for the oxidation: the scale thickness for oxidation under a P_{O2} of 10^{5} Pa is at least twice that under a P_{O2} of 10^{-14} Pa. Some of the crystals grown on the oxide scales under the higher P_{O2} are considered to be $(Co,Ni)(Al,Cr)_2O_4$, as shown in Fig. 1 and Table 1. It is well known that the morphology of theta-Al_2O_3 consists of blade-like crystals (known as whiskers). In addition, when theta-Al_2O_3 survives for a long time at high temperatures, this oxide crystal grows outward about an order of magnitude faster than alpha-Al_2O_3 (Tolpygo et al., 2000). Therefore, since the theta-phase exists longer under a higher P_{O2}, the oxide has longer whiskers than those transformed earlier, resulting in the formation of an oxide scale with a rougher surface.

Figure 4 shows the SIMS depth profiles of selected elements through the CoNiCrAlY coats of the samples oxidized at 1323 K for 600 min under P_{O2} of 10^{-14} and 10^{5} Pa, respectively. For the oxidation under a P_{O2} of 10^{-14} Pa (Fig. 4(a)), chromium, cobalt, and nickel are concentrated near the surface of the scale, which consists of only the crystalline alpha-Al_2O_3 phase, and high-purity alpha-Al_2O_3 is formed near the scale side of the interface between the scale and alloy. Chromium in the scale formed under a lower P_{O2} should be oxidized to form a solid solution of alpha-$(Al,Cr)_2O_3$, whereas both cobalt and nickel detected in the subsurface should segregate as metals, as shown in Figs. 1 and 2. For oxidation under a P_{O2} of 10^{5} Pa (Fig. 4(b)), the concentrations of chromium, cobalt, and nickel in the scale are considerably higher than those under a P_{O2} of 10^{-14} Pa, and such a high-purity alpha-Al_2O_3 layer evidently does not exist at the interface between the scale and alloy.

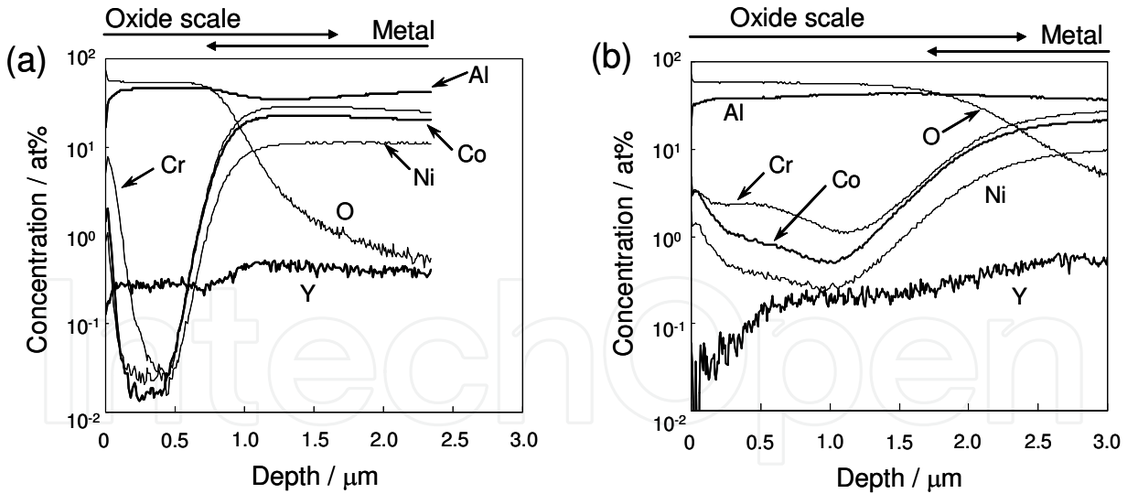

Fig. 4. SIMS depth profiles of selected elements through the CoNiCrAlY coats of the samples oxidized at 1323 K for 600 min under a P_{O2} of (a) 10^{-14} and (b) 10^{5} Pa.

We have evaluated the oxygen permeability of polycrystalline alpha-Al_2O_3 wafers exposed to steep oxygen potential gradients at high temperatures to investigate complicated mass-transfer phenomena through the alpha-Al_2O_3 scale formed on the alloy, as discussed later (Matsudaira et al., 2008, 2010, Wada et al., 2008, Kitaoka et al., 2009). Diffusion of aluminum and oxygen species, which were responsible for the oxygen permeation along the grain boundaries of alpha-Al_2O_3, was found to be strongly dependent on P_{O2}, forming oxygen potential gradients.

When the wafer was subjected to potential gradients caused by a combination of low P_{O2} values, oxygen permeation primarily occurred by grain boundary diffusion of oxygen through oxygen vacancies from the higher P_{O2} surface to the lower P_{O2} surface. Grain boundary ridges were hardly formed on the surfaces under higher P_{O2} because of the very low aluminum flux. Thus, oxidation of CoNiCrAlY through the alpha-Al_2O_3 scale under a P_{O2} of below 10^{-14} Pa is thought to be mainly controlled by inward grain boundary diffusion of oxygen, because oxidation progressed without grain boundary ridges in similar to oxidation under purified argon (Nychka et al., 2005). Nevertheless, chromium, cobalt, and nickel are concentrated near the scale surface formed by oxidation under a P_{O2} of 10^{-14} Pa, as shown in Fig. 4(a). The reason for the segregation of these elements near the scale surface is discussed below.

Figure 5 shows the thermodynamic equilibrium phase boundary (solid line) between alpha-$(Al,Cr)_2O_3$ and $(Cr,Ni)(Al,Cr)_2O_4$ as a function of T^{-1}. Lower oxidation temperature results in a larger stability region for $(Co,Ni)(Al,Cr)_2O_4$. Broken line (A) in Fig. 5 indicates the transition of P_{O2} in the furnace as the temperature increased during oxidation treatment under a P_{O2} of 10^{-14} Pa at 1323 K, corresponding to the testing conditions of Fig. 4(a). The segregation of both cobalt and nickel near the scale surface shown in Fig. 4(a) seems to be caused by initial oxidation during temperature increase to produce $(Co,Ni)(Al,Cr)_2O_4$, followed by reduction and decomposition to cobalt, nickel, and alpha-$(Al,Cr)_2O_3$. According to Fig. 2, the surface segregation of chromium may be thermodynamically promoted by reducing the solubility of chromium ions in the alpha-phase with decreasing oxygen chemical potential in the scale from the scale surface to the interface between the scale and the alloy.

In TBC systems, if a topcoat such as yttria-stabilized zirconia is coated on the pre-oxidized bond coat of CoNiCrAlY, where metallic cobalt and nickel are segregated near the surface of the alpha-$(Al,Cr)_2O_3$ scale on the alloy (Fig. 4(a)), these segregated metals will react with alpha-$(Al,Cr)_2O_3$ in the scale to produce $(Co,Ni)(Al,Cr)_2O_4$ in oxidizing environments at high temperatures, promoting the spalling of TBCs. If the oxidation of the alloy is carried out under a P_{O2} exactly controlled according to broken line (B) in Fig. 5, which indicates the transition of P_{O2} in the furnace when the temperature is increasing, production of $(Co,Ni)(Al,Cr)_2O_4$ at low temperatures will be inhibited. In other words, although the thickness of the scale formed along line (B) in Fig. 5 will be similar to that formed along line (A) in Fig. 5, the surface segregation of cobalt and nickel in the alpha-$(Al,Cr)_2O_3$ scale will be suppressed.

The SIMS depth profiles of cobalt and nickel through the CoNiCrAlY coats of the samples oxidized at a holding temperature of 1323 K under a P_{O2} of 10^{-14} Pa are shown in Fig. 6. Lines (a) and (b) in Fig. 6 are when the temperature was increased to 1323 K according to the P_{O2} along line (A) in Fig. 5 and then held at 1323 K for 10 and 600 min, respectively. Line (c) in Fig. 6 is when the temperature was increased up to 1323 K according to the P_{O2} along line (B) in Fig. 5 and then held for 600 min. When the samples were treated during oxidation under the P_{O2} along line (A) in Fig. 5, only varying the holding time at 1323 K, the concentration depths of both cobalt and nickel near the scale surface are constant and independent of the holding time, as shown by lines (a) and (b) of Fig. 6. Because the oxidation treatments use the same P_{O2} transition and heating rate when the temperature was increased, the amount of $(Co,Ni)(Al,Cr)_2O_4$ produced at lower temperature was thought to be constant and did not depend on the holding time at 1323K. As shown in Fig. 6(c), when P_{O2} during the temperature increase in the oxidation treatment is reduced in the manner indicated by line (B) in Fig. 5, concentrations of cobalt and nickel at the top surface of the scale are decrease to about 1/10 those under the P_{O2} indicated by line (A) in Fig. 5. The lower P_{O2} during the temperature increase in the oxidation treatment is, the lower surface

concentrations of these elements are, and monolithic alpha-$(Al,Cr)_2O_3$ scale will certainly form. It is expected that the adherence between the topcoat and bond coat will be considerably improved by controlling the P_{O2} transition during the temperature increase, resulting in further improvement in the durability of TBC systems.

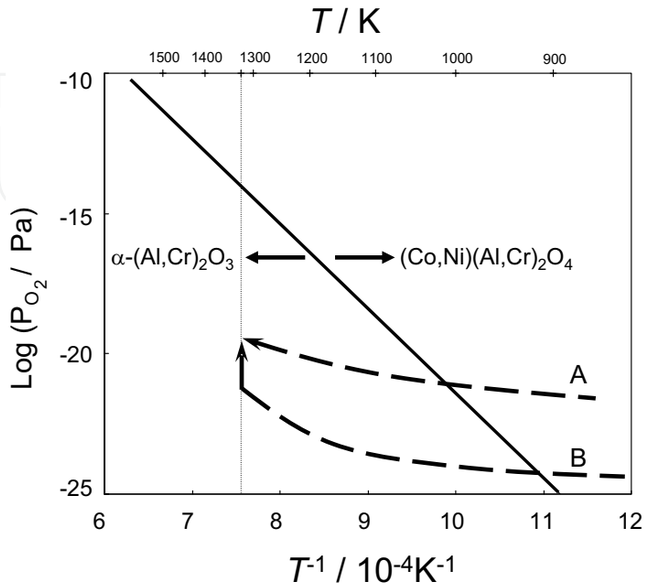

Fig. 5. Thermodynamic equilibrium phase boundary line (solid line) between alpha-$(Al,Cr)_2O_3$ and $(Cr,Ni)(Al,Cr)_2O_4$ as a function of T^{-1}. The broken lines A and B in Fig. 5 indicate the transition of P_{O2} in the furnace during the temperature increase in the oxidation treatment under a P_{O2} of 10^{-14} Pa at 1323 K.

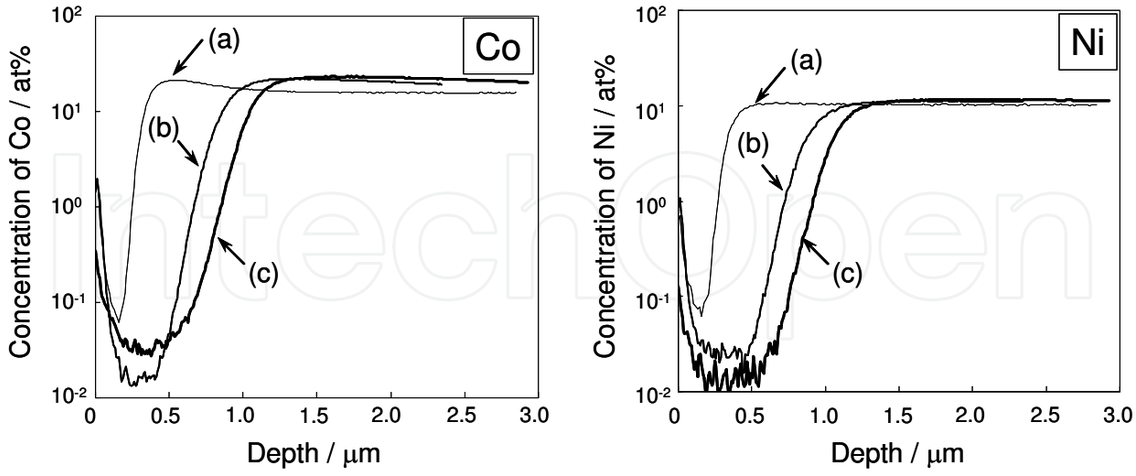

Fig. 6. SIMS depth profiles of Co and Ni through the CoNiCrAlY coats of the samples oxidized at a holding temperature of 1323 K under a P_{O2} of 10^{-14} Pa. Lines (a) and (b) in Fig. 8 are when the temperature was increased to 1323 K according to P_{O2} along line A in Fig.5 and then held for 10 and 600 min, respectively. Line (c) in Fig. 6 is when the temperature was increased to 1323 K according to P_{O2} along line B in Fig. 5 and then held for 600 min.

3. Mass-transfer of Al_2O_3 polycrystals under oxygen potential gradients

3.1 Experimental procedures

3.1.1 Materials

Commercial, high-purity alumina powder (TM-DAR, Taimei Chemicals Co., Ltd., Nagano, Japan, purity > 99.99 wt%) was used for the undoped alumina. Lutetia-doped powders (0.2 mol% of Lu_2O_3) were also prepared by mixing the alumina powder and an aqueous solution of lutetium nitrate hydrate ($Lu(NO)_3 \cdot xH_2O$ (>99.999%), Sigma-Aldrich Co., MO, USA) and subsequent drying to remove the water solvent. Each powder was molded by a uniaxial press at 20 MPa and then subjected to cold isostatic pressing at 600 MPa. The green compacts were pressureless sintered in air at 1773 K for 5 h. Wafers with dimensions of diameter 23.5×0.25 mm were cut from the sintered bodies and then polished so that their surfaces had a mirror-like finish. The relative density of the wafers was 99.5% of the theoretical density. All the wafers had similar microstructures with an average grain size of about 10 micrometer.

3.1.2 Oxygen permeability constants

Figure 7 shows a schematic diagram of the oxygen permeability apparatus. A polycrystalline alpha-Al2O3 wafer was set between two alumina tubes in a furnace. Platinum gaskets were used to create a seal between the wafer and the Al_2O_3 tubes by loading a dead weight from the top of the upper tube. A gas-tight seal was achieved by heating at 1893-1973 K under an Ar gas flow for 3 hrs or more. After that, a P_{O2} of oxygen included as an impurity in the Ar gas was monitored at the outlets of the upper and lower chambers that enclosed the wafer and the Al_2O_3 tubes using a zirconia oxygen sensor at 973K. The partial pressure of water vapor (P_{H2O}) was measured at room temperature using an optical dew point sensor. These measured P_{O2} and P_{H2O} were regarded as backgrounds. Then, pure O_2 gas or Ar gas containing either 1-10 vol% O_2 or 0.01-1 vol% H_2 was introduced into the upper chamber at a flow rate of 1.67×10^{-6} m^3/s. A constant flux for oxygen permeation was judged to be achieved when the values of the P_{O2} and P_{H2O} monitored in the outlets became constant.

When either O_2 gas or the Ar/O_2 mixture was introduced into the upper chamber and Ar was introduced into the lower chamber to create an oxygen gradient across the wafer, oxygen permeated from the upper chamber to the lower chamber. The P_{O2} values in the lower chamber at the experimental temperatures were calculated thermodynamically from the values measured at 973 K. The calculated values were almost the same as those at 973 K. On the other hand, when the Ar/H_2 mixture was introduced into the upper chamber and Ar was introduced into the lower chamber, a tiny amount of oxygen in the Ar permeated from the lower chamber to the upper chamber and reacted with H_2 to produce water vapor. As a result, the P_{H2O} in the upper chamber increased while the H_2 partial pressure (P_{H2}), which was measured at room temperature by gas chromatography, in the upper chamber decreased. The increase of P_{H2O} in the upper chamber was comparable to the reduction of P_{O2} in the lower chamber in terms of oxygen, and the P_{H2O} in the lower chamber remained constant during the permeation tests; thus, hydrogen permeation from the upper chamber to the lower chamber was negligibly small in comparison with the oxygen permeation in the opposite direction. The P_{O2} values in the upper chamber at the experimental temperatures were estimated thermodynamically from the P_{H2O} and P_{H2} measured at room temperature.

The oxygen permeability constant, PL, was calculated from the difference between the P_{O2} estimated thermodynamically in one chamber (which had a lower P_{O2} than that in another chamber) and the background in the lower P_{O2} chamber using [20), 22), 23)]

$$PL = \frac{C_p \cdot Q \cdot L}{V_{st} \cdot S}, \tag{1}$$

where C_p is the concentration of permeated oxygen (P_{O2}/P_T, where P_T = total pressure), Q is the flow rate of the test gases, V_{st} is the standard molar volume of an ideal gas, S is the permeation area of the wafer, and L is the wafer thickness.

The wafer surfaces exposed to oxygen potential gradients at 1923 K for 10 hrs were observed by scanning electron microscopy (SEM) combined with energy dispersive spectroscopy (EDS), and X-ray diffraction (XRD). The volume of the grain boundary ridges formed on the surfaces by the oxygen potential gradients was measured by 3D laser scanning microscopy, and was compared with the total amount of the oxygen permeated in the wafer.

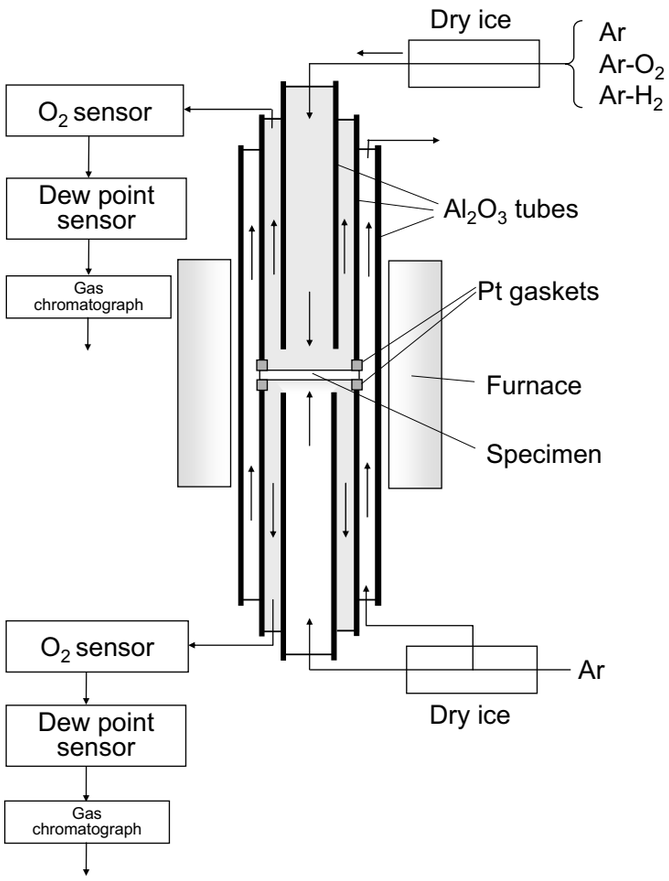

Fig. 7. Schematic diagram of the gas permeability apparatus.

3.1.3 Determination of grain boundary diffusion coefficients

(a) Fluxes of charged particles

The charged particle flux is described as

$$J_i = -Z_i \left(\frac{C_i D_i}{RT} \right) \frac{\partial \eta_i}{\partial x}, \tag{2}$$

where Z_i is the charge of the diffusing particle, C_i is the molar concentration per unit volume, D_i is the diffusion coefficient, R is the gas constant, T is the absolute temperature, x is a space coordinate, and η_i is the electrochemical potential.
The flux of oxygen that permeates through the wafer is equal to the sum of J_{Al} and J_O,

$$J_{TO} = J_{Al} + J_O = -\left(\frac{Z_{Al}^2}{Z_O} C_{Al} D_{Al} + Z_O C_O D_O \right) \frac{(t_{h^\cdot} + t_{e'})}{RT} \cdot \frac{\partial \mu_O}{\partial x} \tag{3}$$

where t_i is the transport number and μ_O is the oxygen chemical potential.
Integrating Eq. (3) from x = 0 to x = L gives

$$\int_0^L J_{TO} dx = -\frac{(t_{h^\cdot} + t_{e'})}{2} \left(\frac{Z_{Al}^2 C_{Al}}{Z_O} \int_{P_{O_2}(I)}^{P_{O_2}(II)} D_{Al} d \ln P_{O_2} + Z_O C_O \int_{P_{O_2}(I)}^{P_{O_2}(II)} D_O d \ln P_{O_2} \right) \tag{4}$$

Equation (4) is applicable to the case of ideal oxygen permeation when there is no interaction between electrons and holes, or when either electrons or holes exclusively participate (Kitaoka et al., 2009, Matsudaira et al., 2010).

(b) Oxygen grain boundary diffusion

The flux of oxygen that permeates through the wafer is postulated to be equal only to J_O. It is also assumed that oxygen permeates only through reactions between defects, in which both oxygen vacancies and electrons participate. In these reactions, dissociative adsorption of O_2 molecules is assumed to progress on the surface exposed to the higher P_{O2} (i.e., $P_{O2}(II)$) as follows.

$$1/2O_2 + V_O^{\cdot\cdot} + 2e' \rightarrow O_O^X \tag{5}$$

Oxygen ions migrate through oxygen vacancies from the $P_{O2}(II)$ side to the lower P_{O2} side (i.e., $P_{O2}(I)$), and oxygen vacancies and electrons diffuse in the opposite direction to the oxygen flux. The inverse reaction to Eq. (5) proceeds on the $P_{O2}(I)$ surface, and oxygen ions recombine to produce O_2 molecules.
If the diffusing species migrate mainly along the grain boundaries of polycrystalline Al_2O_3, the grain boundary diffusion coefficient of oxygen related to Eq. (5), is written as

$$D_{Ogb}\delta = \frac{D_{V_{Ogb}^{\cdot\cdot}}}{C_{Ob} S_{gb}} \left(\frac{1}{4K_{V_{Ogb}^{\cdot\cdot}}} \right)^{1/3} P_{O_2}^{-1/6} = -\frac{A_O}{6 C_{Ob} S_{gb}} P_{O_2}^{-1/6} \tag{6}$$

where D_{Ogb} is the grain boundary diffusion coefficient of oxygen, δ is the grain boundary width, C_{Ob} is the molar concentration of oxygen per unit volume, S_{gb} is the grain boundary density, which is determined from the average grain size in the Al_2O_3. $D_{V_{Ogb}^{\cdot\cdot}}$ is the grain boundary diffusion coefficient of an oxygen vacancy and $K_{V_{Ogb}^{\cdot\cdot}}$ is the equilibrium constant of reaction (5) that occurs at grain boundaries. Assuming that $t_{e'} = 1$ and $D_{Ogb} >> D_{Algb}$, and inserting $Z_O = -2$ and Eq. (6) into Eq. (4) gives

$$\int_0^L J_{TO}dx = A_O(P_{O_2}(II)^{-1/6} - P_{O_2}(I)^{-1/6}) = 4PL \quad (7)$$

If the constant A_O is determined experimentally using Eq. (7), $D_{Ogb}\delta$ for a certain P_{O2} can be estimated from Eq. (6).

(c) Aluminum grain boundary diffusion

The flux of oxygen that permeates through the wafer is premised to be equal only to J_{Al}. Oxygen permeation is also assumed to occur by reactions in which both aluminum vacancies and holes participate. O_2 molecules are absorbed on the surface exposed to $P_{O2}(II)$ as follows.

$$1/2O_2 \rightarrow O_O^X + 2/3V_{Al}^{'''} + 2h^{\bullet} \quad (8)$$

Aluminum vacancies move from the $P_{O2}(II)$ side to the $P_{O2}(I)$ side, and aluminum ions and holes migrate in the opposite direction. Finally, the inverse reaction of (8) occurs on the $P_{O2}(I)$ surface, and oxygen ions recombine to produce an O_2 molecule.

In a similar way to Section 3.1.3(b), the grain boundary diffusion coefficient of aluminum, D_{Algb}, is obtained as follows.

$$D_{Algb}\delta = \frac{D_{V'''_{Algb}}}{C_{Alb}S_{gb}}\left(\frac{K_{V'''_{Algb}}}{9}\right)^{3/8} P_{O_2}{}^{3/16} = \frac{A_{Al}}{12C_{Alb}S_{gb}} P_{O_2}{}^{3/16} \quad (9)$$

C_{Alb} denotes the molar concentration of aluminum per unit volume, $D_{V'''_{Algb}}$ is the grain boundary diffusion coefficient of aluminum vacancies, $K_{V'''_{Algb}}$ is the equilibrium constant of reaction (8) that occurs at the grain boundaries. If it is assumed that $t_h{}^{\bullet}$=1 and $D_{Algb} >> D_{Ogb}$, then substituting Z_{Al} = +3 and Z_O = -2 into Eq. (4) gives

$$\int_0^L J_{TO}dx = A_{Al}(P_{O_2}(II)^{3/16} - P_{O_2}(I)^{3/16}) = 4PL \quad (10)$$

If the experimental value of A_{Al} is obtained using Eq. (10), $D_{Algb}\delta$ for a certain P_{O2} can be calculated from Eq. (9).

3.2 Oxygen permeation

Figure 8 shows the temperature dependence of oxygen permeability constant of polycrystalline Al_2O_3 (non-doped and doped with 0.2 mol% Lu_2O_3) exposed to oxygen potential gradients (ΔP_{O2}). The solid and open symbols indicate data for specimens exposed under $P_{O2}(II)/P_{O2}(I)$= 1 Pa/10^{-8} Pa and 10^5 Pa/1 Pa, respectively. The other lines are data from the literature under a similar ΔP_{O2} as that for the open symbols. The oxygen permeability constants are found to increase with increasing temperature, such that they are proportional to T^{-1}, in a similar manner as the data from the literature. The oxygen permeability constants tend to decrease with increasing purity of Al_2O_3. For $P_{O2}(II)/P_{O2}(I)$ = 10^5 Pa/1 Pa, the oxygen permeability constants of the lutetia-doped wafer are similar to those of the undoped wafer. Although the slopes of the curves for $P_{O2}(II)/P_{O2}(I)$ = 1 Pa/10^{-8} Pa are the same for both samples, they are markedly different from those for $P_{O2}(II)/P_{O2}(I)$= 10^5 Pa/1 Pa. Furthermore, the permeability constants obtained for $P_{O2}(II)/P_{O2}(I)$ = 1 Pa/10^{-8} Pa

are clearly reduced by lutetia doping. These results suggest that the effect of lutetia doping on the oxygen permeation and the corresponding permeation mechanism vary depending on the oxygen potential gradients.

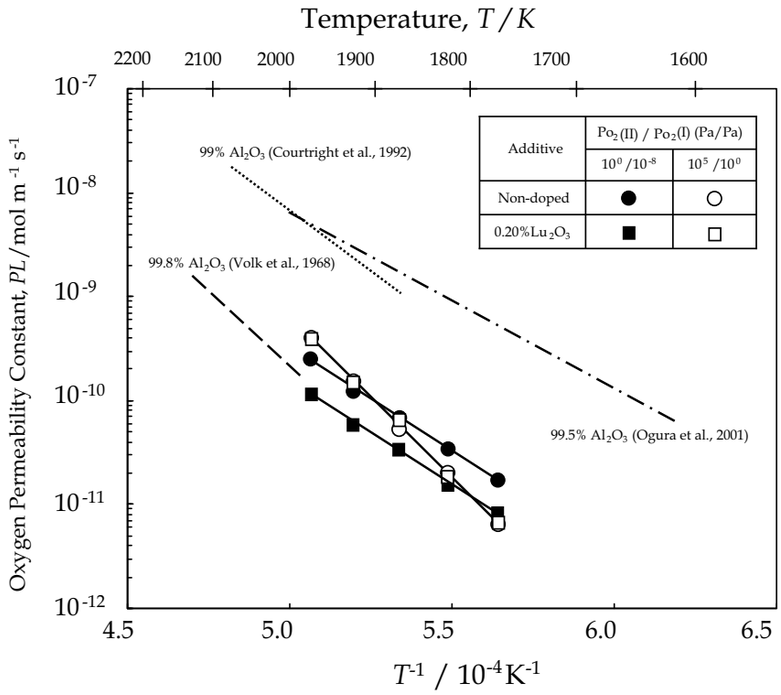

Fig. 8. Temperature dependence of oxygen permeability constant of polycrystalline Al_2O_3 (non-doped and doped with 0.2 mol% Lu_2O_3) exposed to oxygen potential gradients (ΔP_{O2}). The solid and open symbols indicate data for specimens exposed under P_{O2}(II)/ P_{O2}(I)= 1 Pa/10^{-8} Pa and 10^5 Pa/1 Pa, respectively. The other lines are data from the literature under a similar ΔP_{O2} as that for the open symbols.

Because the oxygen permeability constants of a single-crystal Al_2O_3 wafer were lower than the measurable limit of this system (below 1×10^{-12} mol·m^{-1}s^{-1} at 1773 K), the oxygen permeation is thought to occur preferentially through the grain boundaries for the polycrystalline Al_2O_3 (Matsudaira et al., 2008). Furthermore, the oxygen permeability constants of the polycrystalline wafers were inversely proportional to the wafer thickness. According to Eq.(2), therefore, the oxygen permeation is considered to be controlled by diffusion in the wafer, not by interfacial reaction between the wafer surfaces and ambient gases.

Figure 9 shows the effect of P_{O2} under a steady state in the upper chamber on the oxygen permeability constants of polycrystalline alumina (undoped and doped with 0.20 mol% Lu_2O_3) at 1923 K, where the P_{O2} in the lower chamber is constant at about 1 Pa. For P_{O2} values of less than 10^{-3} Pa, the oxygen permeability constants decrease with increasing P_{O2} for both the undoped and lutetia-doped wafers. The slopes of the curves correspond to a power constant of n = -1/6, which is applicable to the defect reaction given in Eq. (5) and is related to P_{O2}(I) in accordance with Eq. (7), since P_{O2}(II) >> P_{O2}(I). O_2 molecules are assumed to permeate mainly by grain boundary diffusion of oxygen through the oxygen vacancies from the higher to the lower P_{O2} surface. When the doping level is 0.2 mol%, the oxygen

permeability constants are about three times smaller than for undoped alumina, although the slopes of the curves are similar. Thus, lutetium doping seems to suppress the mobility of oxygen without changing the oxygen diffusion mechanism. On the other hand, the oxygen permeability constants for all the polycrystals for P_{O2} values above 10^3 Pa in the upper chamber are similar to each other and increase with increasing P_{O2}, as shown in Fig. 9. Their slopes correspond to a power constant of n = 3/16 that suggests participation in the defect reaction given in Eq. (8) and P_{O2}(II) in accordance with Eq. (10), since P_{O2}(II) >> P_{O2}(I). Under potential gradients generated by P_{O2} values above approximately 10^3 Pa, O_2 molecules seem to permeate mainly by grain boundary diffusion of aluminum through aluminum vacancies from the lower to the higher P_{O2} surface. In this case, the lutetium segregated at grain boundaries would be expected to have little effect on the diffusivity of aluminum.

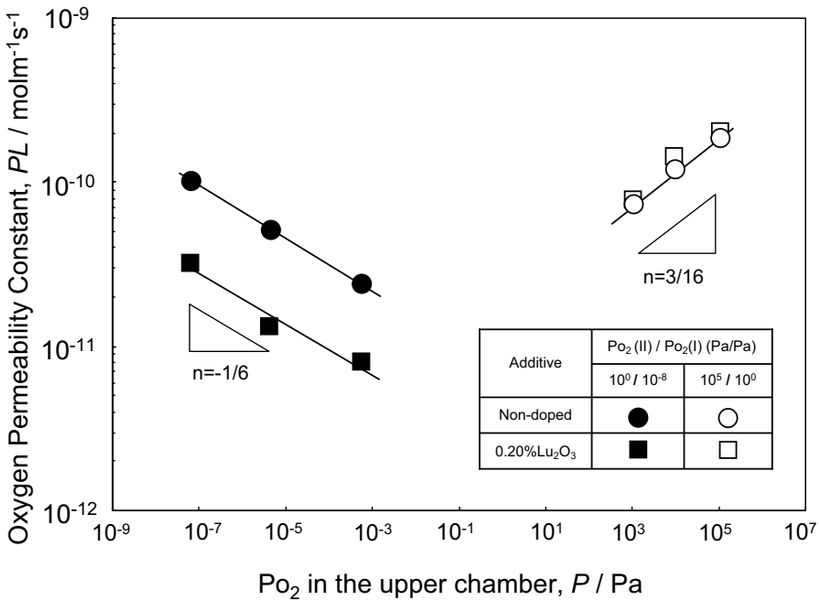

Fig. 9. Effect of P_{O2} in the upper chamber on the oxygen permeability constants of polycrystalline alumina (non-doped and doped with 0.2 mol% Lu_2O_3) at 1923 K. The solid symbols indicate data for specimens exposed to a ΔP_{O2} between about P_{O2}(II) = 1 Pa in the lower chamber and a much lower P_{O2} (P_{O2}(I)) in the upper chamber. The open symbols indicate data for specimens exposed to a ΔP_{O2} between P_{O2}(I) = 1 Pa in the lower chamber and a much higher P_{O2} (P_{O2}(II)) in the upper chamber.

Figure 10 shows SEM micrographs of the surfaces and cross-sections of non-doped polycrystalline alumina exposed at 1923 K for 10 h under ΔP_{O2} with P_{O2}(II)/ P_{O2}(I)= 1 Pa/10^{-8} Pa and 10^5 Pa/1 Pa. For P_{O2}(II)/ P_{O2}(I)= 1 Pa/10^{-8} Pa, grain boundary grooves are observed on both the surfaces, of which morphology is similar to that formed by ordinary thermal etching. The oxygen potential gradients with combination of the lower P_{O2} values hardly affect the surface morphological change. The absence of the grain boundary ridges suggests that the migration of aluminum was scarcely related to the oxygen permeation. This surface morphology supports the oxygen permeation mechanism with n = -1/6 as shown in Fig. 9. For P_{O2}(II)/ P_{O2}(I)= 10^5 Pa/1 Pa, grain boundary ridges with heights of a few micrometers

can be seen on the P_{O2}(II) surface, while deep crevices are formed at the grain boundaries on the P_{O2}(I) surface. The total volume of the grain boundary ridges, measured by 3D laser scanning microscopy, was consistent with the volume of alumina that should be produced given the observed amount of oxygen permeation (Kitaoka et al., 2009). This result provides adequate support for an oxygen permeation mechanism with n = 3/16, as shown in Fig. 9.

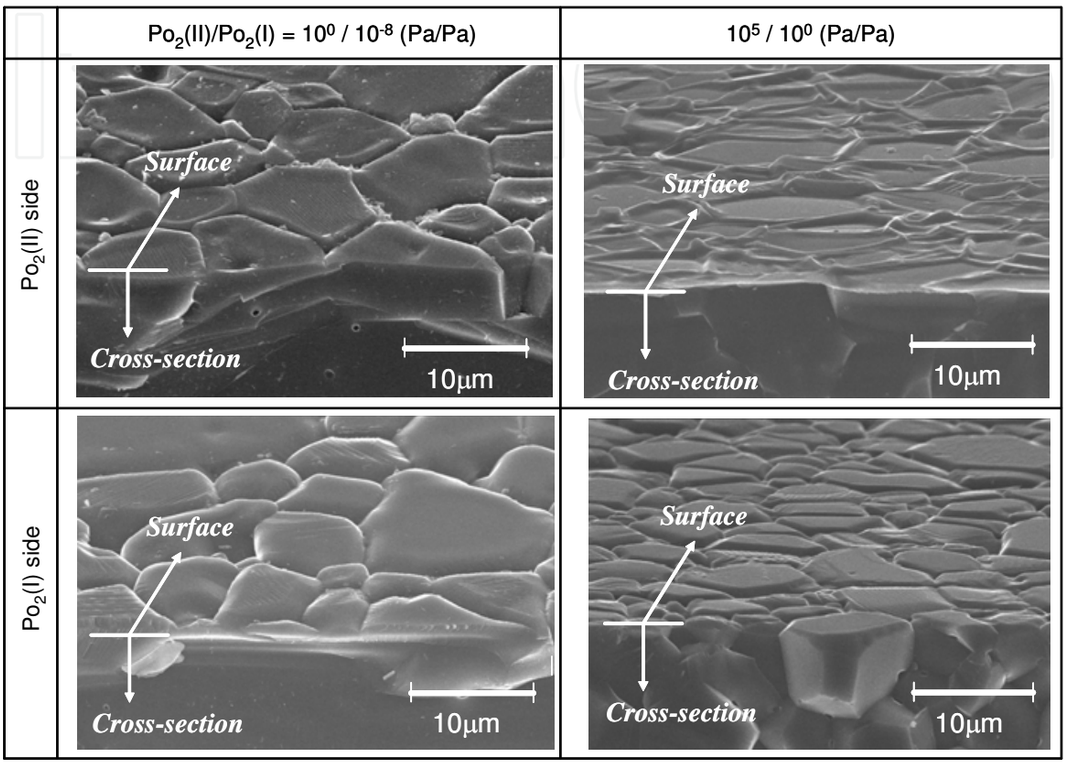

Fig. 10. shows SEM micrographs of the surfaces and cross-sections of non-doped polycrystalline alumina exposed at 1923K for 10h under ΔP_{O2} with P_{O2}(II)/P_{O2}(I)=1 Pa/10^{-8} Pa and 10^5 Pa/1 Pa.

Figure 11 shows SEM micrographs of the surfaces and cross-sections of polycrystalline alumina doped with 0.2 mol% Lu_2O_3 exposed at 1923 K for 10 h under ΔP_{O2} with P_{O2}(II)/ P_{O2}(I)= 1 Pa/10^{-8} Pa and 10^5 Pa/1 Pa. Figure 12 shows top-view SEM images of the surfaces corresponding to Fig. 11. In the case of P_{O2}(II)/ P_{O2}(I) = 1 Pa/10^{-8} Pa, as shown in Fig. 11, shallow grain boundary grooves, similar to those produced by conventional thermal etching, are observed on both surfaces, as in the case of undoped alumina. In addition, as seen in Fig. 12, a large number of particles with diameters of about 1 micrometer are uniformly distributed at the grain boundaries on both surfaces. The distribution of the particles was maintained during exposure under the oxygen potential gradient at 1923 K. These particles were identified as $Al_5Lu_3O_{12}$ by XRD and EDS and had already precipitated at the grain boundaries by reaction of alumina grains with excess lutetium during sintering the sample. The remainder of the added lutetium should then become segregated at the grain boundaries. This implies that the lutetium species scarcely migrates, remaining in the wafer during oxygen permeation, and inhibiting the mobility of oxygen from the region of higher P_{O2} to the region of lower P_{O2} (Fig. 9).

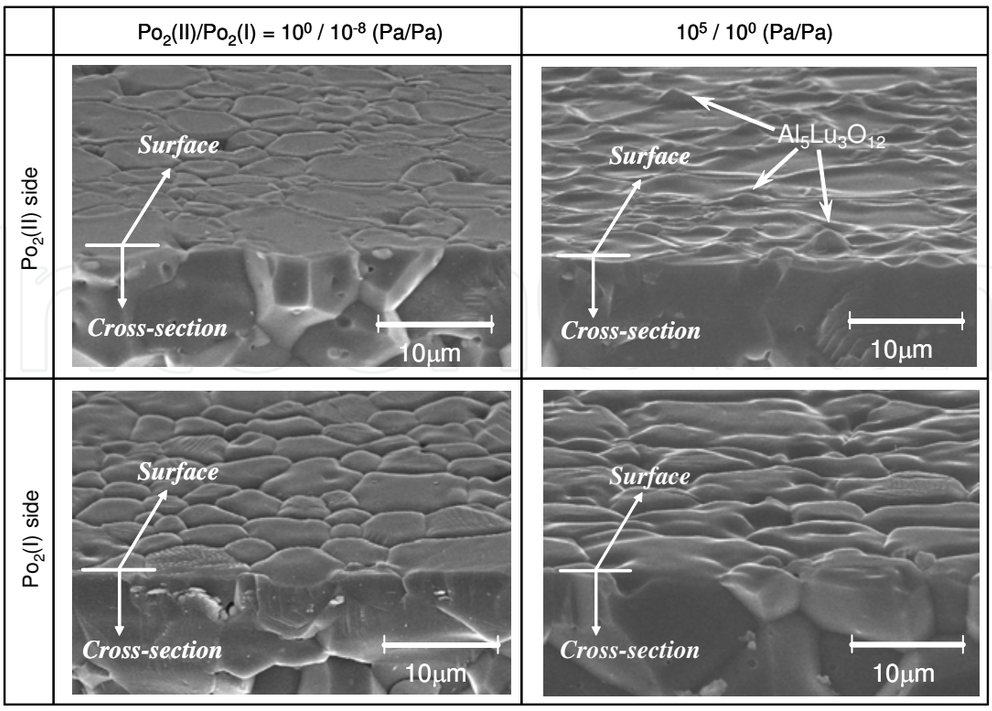

Fig. 11. SEM micrographs of the surfaces and cross-sections of polycrystalline alumina doped with 0.2 mol% Lu_2O_3 exposed at 1923 K for 10 h under ΔP_{O2} with $P_{O2}(II)/ P_{O2}(I)= 1$ Pa/10^{-8} Pa and 10^5 Pa/1 Pa.

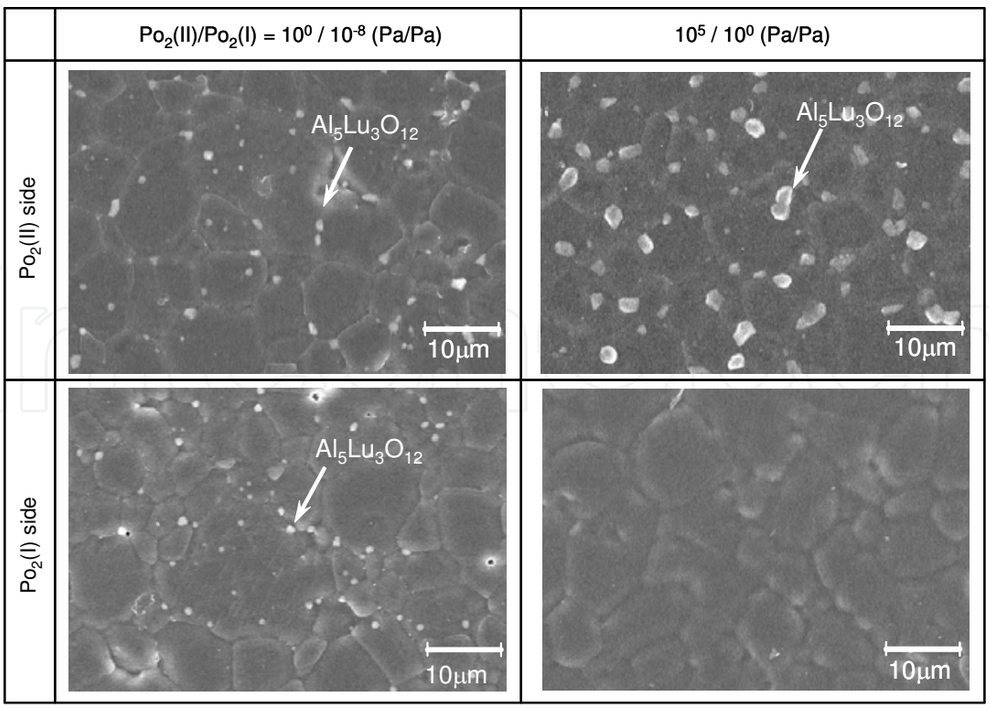

Fig. 12. SEM micrographs of the surfaces of polycrystalline alumina doped with 0.2 mol% Lu_2O_3 exposed at 1923K for 10h under ΔP_{O2} with $P_{O2}(II)/P_{O2}(I)$=1 Pa/10^{-8}Pa and 10^5Pa/1Pa.

For P_{O2}(II)/ P_{O2}(I) = 10^5 Pa/1 Pa, Fig. 11 reveals that the grain boundaries on the higher P_{O2} surface are raised to a height of a few micrometer, while deep trenches are formed at the grain boundaries on the lower P_{O2} surface, similar to the case for undoped alumina. Furthermore, as seen in Fig. 12, the higher P_{O2} surface exhibits $Al_5Lu_3O_{12}$ particles with diameters of several micrometer, but such particles are not found on the opposite surface. This can be explained by a migration of both lutetium and aluminum from the lower to the higher P_{O2} region.

3.3 Grain boundary diffusion coefficients

The grain boundary diffusion coefficients of oxygen and aluminum ($D_{gb}\delta$) are estimated from the oxygen permeability constants shown in Fig.9 by the procedure described in Section 3.1.3. Figure 13 shows $D_{gb}\delta$ for oxygen and aluminum in polycrystalline alumina (undoped and doped with 0.20 mol% Lu_2O_3) as a function of the equilibrium partial pressure of oxygen in the upper chamber at 1923 K. Values of oxygen diffusion coefficients

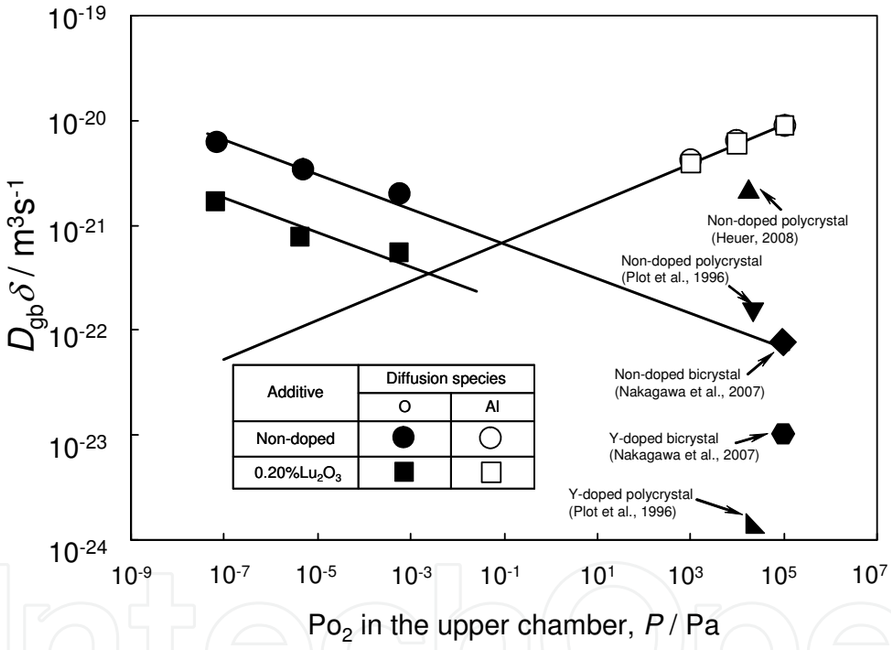

Fig. 13. $D_{gb}\delta$ of oxygen and aluminum in polycrystalline alumina (non-doped and doped with 0.2 mol% Lu_2O_3) as a function of the equilibrium partial pressures of oxygen in the upper chamber at 1923 K. The solid and open symbols indicate the $D_{gb}\delta$ of oxygen and aluminum, respectively.

taken from the literature (Plot et al., 1996, Nakagawa et al., 2007, Heuer, 2008) are also shown in Fig. 13. They were determined using an ^{18}O isotopic tracer profiling technique for bicrystalline or polycrystalline alumina annealed in a homogeneous environment in the absence of an oxygen potential gradient, and their P_{O2} values on the abscissa correspond to those in the annealing environments. The data for refs. (Nakagawa et al., 2007, Heuer, 2008) are estimated by extrapolating to 1923 K. For lutetia-doped polycrystalline alumina, there are unfortunately no data for oxygen grain boundary diffusion coefficients determined by

the tracer profiling technique, but some measurements have been carried out on yttria-doped alumina. On the other hand, it has been reported that creep resistance in polycrystalline alumina was improved remarkably by doping to only 0.05-0.1 mol% with oxides such as Lu_2O_3 and Y_2O_3 in a similar effect on the creep resistance to each other (Ikuhara et al., 2001). Thus, the grain boundary coefficients for oxygen in yttria-doped alumina (polycrystal and bicrystal) are shown in Fig. 13 for reference.

The $D_{gb}\delta$ value for oxygen is seen to decrease with increasing P_{O2}, whereas the value for aluminum increases for both undoped and lutetia-doped alumina. Increasing the doping level to 0.2 mol% lutetia causes an approximately three times reduction in $D_{gb}\delta$, while maintaining the slope of the curve. In contrast, the $D_{gb}\delta$ value of aluminum is unaffected by lutetia doping. Thus, lutetia doping has the effect of reducing the mobility of oxygen along the grain boundaries, but has little influence on the diffusion of aluminum.

For the undoped alumina, the line extrapolated to higher P_{O2} for $D_{gb}\delta$ of oxygen is consistent with previous reported data obtained using SIMS (Plot et al., 1996, Nakagawa et al., 2007), but deviates widely from data using NRA (Heuer, 2008). There is a thermal equilibrium level of defects such as Schottky pairs (Buban et al., 2006) or Frenkel pairs (Heuer, 2008) in alumina held in uniform environments at high temperatures. As shown in Figs. 9-13, the oxygen potential gradients through the wafer seem to result in the formation of new defects such as oxygen vacancies for lower P_{O2} ranges and aluminum vacancies for higher P_{O2} ranges, in addition to the thermally induced defects. Because $D_{gb}\delta$ for oxygen and aluminum are proportional to the concentration of their respective vacancies, the dominant defects in the wafer are probably oxygen vacancies for lower P_{O2} values and aluminum vacancies for higher P_{O2} values. Therefore, the extrapolated line in Fig. 8 may correspond to the SIMS data (Plot et al., 1996, Nakagawa et al., 2007), where the concentration of oxygen vacancies induced by the oxygen potential gradient for the higher P_{O2} ranges is asymptotic to that under thermal equilibrium. Nevertheless, the reason why the NRA result deviates so much cannot be ascertained based on the descriptions given in the paper (Heuer, 2008).

As mentioned above, elements such as yttrium and lutetium that were segregated at the grain boundaries of alumina by addition of only 0.05-0.1 mol% Ln_2O_3 effectively retarded oxygen grain boundary diffusivity, creep deformation and final-stage sintering under uniform environments (Nakagawa et al., 2007, Ikuhara et al., 2002, Yoshida et al., 2002, 2007, Watanabe et al., 2003). Retardation of such mass transfer can be explained by a 'site-blocking' mechanism (Amissah et al., 2007, Wang et al., 1999, Cho et al., 1999, Cheng et al., 2008, Priester, 1989, Korinek et al., 1994) and/or grain boundary strengthening (Yoshida et al., 2002, Buban et al., 2006). Under the oxygen potential gradients used in this study, it was found that oxygen diffusitivity was unaffected by 0.05 mol% lutetia-doping (Matsudaira et al., 2010), and even for 0.2 mol% doping, the retardation was small compared to the effect in uniform environments. This may be related to the generation of a large number of oxygen vacancies in the vicinity of the grain boundaries under an oxygen potential gradient, despite the fact that Lu^{3+} is isovalent with Al^{3+}.

As mentioned in the Introduction, Bedu-Amissah et al. measured Cr^{3+} diffusion in alumina under a Cr^{3+} concentration gradient (Amissah et al., 2007). From the chromium diffusion profile, they found that yttrium doping retards cation diffusion in the vicinity of the grain boundary, reducing $D_{gb}\delta$ by at least one order of magnitude (Amissah et al., 2007). In

contrast, the $D_{gb}\delta$ value of aluminum under oxygen potential gradients is unaffected by lutetia doping. Thus, lutetia doping has little influence on the diffusion of aluminum along grain boundaries. This may be related to the generation of a large number of aluminum vacancies around grain boundaries under an oxygen potential gradient, which reduces the effect of 'site-blocking' and/or grain boundary strengthening, resulting in outward diffusion of both lutetium and aluminum, as shown in Figs. 11 and 12.

4. Conclusions

The oxidation of the CoNiCrAlY alloy under a P_{O2} of 10^{-14} Pa at 1323 K, during which both aluminum and chromium in the alloy were oxidized and elements such as cobalt and nickel were not oxidized, accelerated the transformation from metastable theta-Al_2O_3 to stable alpha-Al_2O_3, resulting in the formation of a dense, smooth alpha-$(Al,Cr)_2O_3$ scale. The surface concentrations of cobalt and nickel in the scale, which was evolved by formation of $(Co,Ni)(Al,Cr)_2O_4$ during the temperature increase and subsequent reduction and decomposition of the oxide at a higher temperature, could be effectively reduced by decreasing the P_{O2} during the temperature rise in the oxidation treatment. By contrast, oxidation at a higher P_{O2} required a longer time for the transformation and $(Co,Ni)(Al,Cr)_2O_4$ was also produced in the scale with a rougher surface.

The oxygen permeability of undoped and lutetia-doped polycrystalline alpha-alumina wafers that were exposed to oxygen potential gradients (ΔP_{O2}) was evaluated at high temperatures to investigate the mass-transfer phenomena through the alumina scale. The main diffusion species during oxygen permeation through the alumina grain boundaries was found to depend on P_{O2} values, which created ΔP_{O2}. Under ΔP_{O2} generated by low P_{O2} values, where oxygen permeation occurred by oxygen diffusion from regions of higher to low P_{O2}, segregated lutetium at the grain boundaries suppressed only the mobility of oxygen in the wafers, without affecting the oxygen permeation mechanism. By contrast, under ΔP_{O2} generated by high P_{O2} values, where oxygen permeation proceeded by aluminum diffusion from regions of lower to higher P_{O2}, lutetium had little effect on aluminum diffusion and migrated together with aluminum, resulting in precipitation and growth of $Al_5Lu_3O_{12}$ particles on the higher P_{O2} surface.

5. References

Evans A. G., Mumm D. R., Hutchinson J. W., Meier G. H. & Pettit F. S. (2001). Mechanisms Controlling the Durability of Thermal Barrier Coatings. *Prog. Mater. Sci.*, 46, 505-553

Brumm M. W. & Grabke H.J. (1992). The Oxidation Behavior of NiAl - I. Phase Transformations in the Alumina Scale During Oxidation of NiAl and NiAl-Cr Alloys. *Corrosion Science*, 33, 1677-1690

Tolpygo V.K. & Clarke D.R. (2000). Microstructural Study of the Theta-Alpha Transformation in Alumina Scales Formed on Nickel-Aluminides. *Microscopy of Oxidation*, 17, 59-70

Tolpygo V.K., Clarke D.R. & Murphy K. S. (2001). The Effect of Grit Blasting on the Oxidation Behavior of Platinum-Modified Nickel-Aluminide Coating. *Metall. Mater. Trans.*, 32A, 1467-1478

Tolpygo V.K. & Clarke D.R. (2005). The Effect of Oxidation Pre-Treatment on the Cyclic Life of EB-PVD Thermal Barrier Coatings with Platinum-Aluminide Bond Coats. *Surf. Coat. Technol.* 200, 1276-1281

Nijdam T.J. & Sloof W.G. (2006). Combined Pre-Annealing and Pre-Oxidation Treatment for the Processing of Thermal Barrier Coatings on NiCoCrAlY Bond Coatings. *Surf. Coat. Technol.*, 201, 3894-3900

Matsumoto M., Hayakawa K., Kitaoka S., Matsubara H., Takayama H., Kagiya Y. & Sugita Y. (2006). The Effect of Preoxidation Atmosphere on Oxidation Behavior and Thermal Cyclic life of Thermal barrier Coatings. *Mater. Sci. Eng.* A 411, 119-125

Matsumoto M., Kato T., Hayakawa K., Yamaguchi N., Kitaoka S. & Matsubara H. (2008). The Effect of Pre-Oxidation Atmosphere on the Durability of EB-PVD Thermal Barrier Coatings with CoNiCrAlY Bond Coats. *Surf. Coat. Technol.*, 202, 2742-2748

Pint A., Treska M. & Hobbs L.W. (1997). The Effect of Various Oxide Dispersions on the Phase Composituin and Morphology of Al_2O_3 Scales Grown on beta-NiAl. *Oxid. Met.*, 47, 1-20

Peng X., Clarke D.R. & Wang F. (2003). Transient-Alumina Transformations during the Oxidation of Magnetron-Sputtered CoCrAl Nanocrystalline. *Oxid. Met.*, 60, 225-240

Clarke D.R. (1998). Epitaxial Phase Transformations in Aluminum Oxide. *Phys. Stat. Sol.*, 166, 183-196

Odaka A., Yamaguchi T., Fujita T., Taruta S. & Kitajima K. (2008). Cation Dopant Effect on Phase Transformation and Microstructural Evolution in M^{2+}-Substituted gamma-Alumina Powders. *J Mater. Sci.*, 43, 2713-2720

Nagano T., Sato K., Saitoh T. & Takahashi S. (2009). Hydrothermal Stability of Mesoporous Ni-Doped gamma-Al_2O_3. *J Ceram. Soc. Jpn.*, 117, 832-835

Kitaoka S., Kuroyama T., Matsumoto M., Kitazawa R. & Kagawa Y. (2010). Control of Polymorphism in Al_2O_3 Scale Formed by Oxidation of Alumina-forming Allys. *Corrosion Science*, 52, 429-434

Nychka J.A. & Clarke D.R. (2005). Quantification of Alumminum Outward Diffusion During Oxidation of FeCrAl Alloys. *Oxid. Metals*, 63, 325-352

Matsudaira T., Wada M., Kitaoka S., Asai T., Miyachi Y. & Kagiya Y. (2008). Gas Permeability of Oxide Ceramics at Ultra-high Temperatures. *J Soc. Mater. Sci. Jpn.*, 57, 532-538

Wada M., Matsudaira T. & Kitaoka S. (2008). Oxygen Permeability and Morphological Stability of Alumina Ceramics under O_2 Potential Gradients at Ultra-High Temperatures. *AMTC Letters*, 1, 34-35

Kitaoka S., Matsudaira T. & Wada M. (2009). Mass-Transfer Mechanism of Alumina Ceramics under Oxygen Potential Graddients at High Temperatures. *Mater. Trans.*, 50, 1023-1031

Volk H.F. & Meszaros F.W. (1968). *Ceramic Micro Structures their Analysis Significance & Production*, ed. by R. M. Fullhrath and J. A. Pask, John Wiley and Sons, New York

Courtright E.L. & Prater J.T. (1992). *Oxygen Permeability of Several Oxides above 1200 deg.C*, US DOE Rep. PNL-SA-20302

Ogura Y., Kondo M., Morimoto T., Notomi A. & Sekigawa T. (2001). Oxygen Permeability of Y_2SiO_5. *Mater. Trans.*, 42, 1124-1130.

Plot D., Gall M.L., Lesage B., Huntz A.M. & Monty C. (1996). Self-diffusion in Alpha-Al_2O_3 IV. Oxygen Grain-boundary Self-diffusion in Undoped and Yttria-doped Alumina Polycrystals.*Philos. Mag. A*, 73, 935-949

Nakagawa T., Sakaguchi I., Shibata N., Matsunaga K., Mizoguchi T., Yamamoto T., Haneda H. & Ikuhara Y. (2007). Yttrium Doping Effect on Oxygen Grain Boundary Diffusion in Alpha-Al_2O_3. *Acta Mater.*, 55, 6627-6633

Messaoudi K., Huntz A.M. & Lesage B. (1998). Diffusion and Growth Mechanism of Al_2O_3 Scales on Ferritic Fe-Cr-Al Alloys. *Mater. Sci. Eng. A*, 247, 248-262

Heuer A.H. (2008). Oxygen and Aluminum Diffusion in Alpha-Al_2O_3 : How Much Do We Really Understand ?. *J Eur. Ceram. Soc.*, 28, 1495-1507

Paladino A.E. & Kingery W.D. (1962). Aluminum Ion Diffusion in Aluminum Oxide. *J Chem. Phys.*, 37, 957-962

Le Gall M., Lesage B. & Bernardini J. (1994). Self-diffusion in Alpha-Al_2O_3 I. Aluminum Diffusion in Single Crystals. *Philos. Mag. A*, 70, 761-773

Amissah K.B., Rickman J.M., Chan H.M. & Harmer M.P. (2007). Grain-boundary Diffusion of Cr in Pure and Y-Doped Alumina. *J Am. Ceram. Soc.*, 90, 1551-1555

Pint B.A., Garratt-Reed A.J. & Hobbs L.W. (1998). Possible Role of the Oxygen Potential Gradient in Enhancing Diffusion of Foreign Ions on Alpha-Al_2O_3 Grain Boundaries. *J Am. Ceram. Soc.* 81, 305-314

Matsunaga K., Tanaka T., Yamamoto T. & Ikuhara Y. (2003). First-principles Calculations of Intrinsic Defects in Al_2O_3. *Phys. Rev. B*, 68, 085110

Ikuhara Y., Yoshida H. & Sakuma T. (2001). Impurity Effects on Grain Boundary Strength in Structural Ceramics. *Mater. Sci. Eng.*, A319-321, 24-30

Yoshida H., Ikuhara Y. & Sakuma T. (2002). Grain Boundary Electronic Structure Related to the High-temperature Creep Resistance in Polycrystalline Al_2O_3. Acta Mater., 50, 2955-2966

Wang C.M., Cargill III G.L., Harmer M.P., Chan H.M. & Cho J. (1999). Atomic Structural Environment of Grain Boundary Segregated Y and Zr in Creep Resistant Alumina from EXAFS. *Acta Mater.*, 47, 3411-3422

Cho J., Wang C.M., Chan H.M., Rickman J.M. & Harmer M.P. (1999). Role of Segregating Dopants on the Improved Creep Resistance of Aluminum Oxide. *Acta Mater.*, 47, 4197-4207

Cheng H., Dillon S.J., Caram H.S., Rickman J.M., Chan H.M. & Harmer M.P. (2008). The Effect of Yttrium on Oxygen Grain-boundary Transport in Polycrystalline Alumina Measured Using Ni Maker Particles. *J Am. Ceram. Soc.*, 91, 2002-2008

Priester L. (1989). Geometrical Speciality and Special Properties of Grain Boundaries. *Rev. Phys.*, 24, 419-438

Korinek S.L. & Dupau F. (1994). Grain Boundary Behavior in Superplastic Mg-doped Alumina with Yttria Codoping. *Acta. Metall. Mater.*, 42, 293-302

Buban J.P., Matsunaga K., Chen J., Shibata N., Ching W.Y., Yamamoto T. & Ikuhara Y. (2006). Grain Boundary Strengthening in Alumina by Rare Earth Impurities. *Science*, 311, 212-215

Matsudaira T., Wada M., Saitoh T. & Kitaoka S. (2010). The Effect of Lutetium Dopant on Oxygen Permeability of Alumina Polycristals under Oxygen Potential Gradients at Ultra-high Temperatures. *Acta Mater.*, 58, 1544-1553

Degterov S. & Pelton A.D. (1996). Critical Evaluation and Optimization of the Thermodynamic Properties and Phase Diagrams of the CrO-Cr_2O_3, CrO-Cr_2O_3-Al_2O_3, and CrO-Cr_2O_3-CaO Systems. *J Phase Equilibria*, 17, 476-487

Ansara I., Dupin N., Lukas H.L. & Sundman B.J. (1997). Thermodynamic Assessment of the Al-Ni System. *Alloys and Compounds*, 247, 20-30

Watanabe S., Yoshida H. & Sakuma T. (2003). Densification Behavior and Grain Boundary Diffusivity in Cation-doped Alumina. *Key Engineering Materials*, 247, 67-70

Yoshida H., Morita K., Kim B.N., Hiraga K., Yamamoto T. & Sakuma T. (2007). estimation of Grain Boundary Diffusivity in Cation-doped Polycrystalline Alumina. *Mater Sci Forum*, 558-559, 997-1002

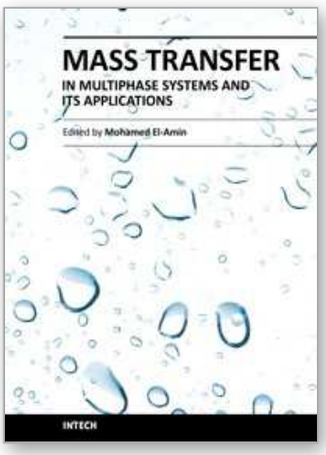

Mass Transfer in Multiphase Systems and its Applications
Edited by Prof. Mohamed El-Amin

ISBN 978-953-307-215-9
Hard cover, 780 pages
Publisher InTech
Published online 11, February, 2011
Published in print edition February, 2011

This book covers a number of developing topics in mass transfer processes in multiphase systems for a variety of applications. The book effectively blends theoretical, numerical, modeling and experimental aspects of mass transfer in multiphase systems that are usually encountered in many research areas such as chemical, reactor, environmental and petroleum engineering. From biological and chemical reactors to paper and wood industry and all the way to thin film, the 31 chapters of this book serve as an important reference for any researcher or engineer working in the field of mass transfer and related topics.

InTech Europe
University Campus STeP Ri
Slavka Krautzeka 83/A
51000 Rijeka, Croatia
Phone: +385 (51) 770 447
Fax: +385 (51) 686 166
www.intechopen.com

InTech China
Unit 405, Office Block, Hotel Equatorial Shanghai
No.65, Yan An Road (West), Shanghai, 200040, China
中国上海市延安西路65号上海国际贵都大饭店办公楼405单元
Phone: +86-21-62489820
Fax: +86-21-62489821

IntechOpen